

Stimulated Raman scattering suppressors fabricated by femtosecond laser overlap-controlled multilayer line-by-line technology

AND YIPING WANG^{1,2}

Abstract: Femtosecond-laser-direct-written fiber gratings suffer from excessive scattering and high insertion loss, which restricts their application in fiber laser systems, particularly in the field of high-power lasers. To address this limitation, we propose an overlap-controlled multilayer line-by-line (OCML-LBL) technique to form planar refractive index modulation (RIM) that covers the fiber core, which can effectively reduce Type II modulation-induced scattering and further minimize insertion loss. Utilizing this approach, we fabricated low-insertion-loss chirped and tilted fiber Bragg grating (CTFBG)-based stimulated Raman scattering (SRS) suppressors and implemented them in a fiber laser system. The fabricated devices demonstrate bandwidths spanning from 38 nm to over 100 nm with efficiencies up to 99.9% at customized wavelengths, and significantly suppress the SRS in the fiber laser. Moreover, the fabricated CTFBG exhibits excellent stability, demonstrating negligible response to temperature, strain, and bending. Owing to its inherent flexibility, this fabrication method holds substantial promise for the customized fiber grating inscription of fiber lasers.

© 2025 Optica Publishing Group under the terms of the Optica Open Access Publishing Agreement

Introduction

Stimulated Raman scattering (SRS) has become one of the critical factors limiting the output performance of fiber lasers. In recent years, the primary devices for suppressing SRS involve long-period fiber gratings (LPFGs) [1,2] and chirped and tilted fiber Bragg gratings (CTFBGs) [3–5], which can filter out undesired SRS signals. However, LPFGs suffer from unstable filtering performance due to their high sensitivity to environmental variables. Conversely, CTFBGs exhibit relatively stable filtering characteristics, leading to their increasing adoption in diverse applications, especially in SRS suppression. As a band-rejection filter, CTFBG can partially couple the forward-propagating core modes into the backward-propagating cladding modes, broadening the spectral bandwidth of these cladding modes and ultimately generating a broad and smooth filtering spectral envelope within a specific wavelength range [6]. Currently, the primary method for fabricating CTFBGs is the ultraviolet (UV) laser phase mask technique, which features technical maturity and enables mass production of gratings with excellent spectral

 $^{^{}m \it l}$ Shenzhen Key Laboratory of Photonic Devices and Sensing Systems for Internet of Things, Guangdong and Hong Kong Joint Research Centre for Optical Fibre Sensors, State Key Laboratory of Radio Frequency Heterogeneous Integration, Shenzhen University, Shenzhen 518060, China

²Shenzhen Key Laboratory of Ultrafast Laser Micro/Nano Manufacturing, Key Laboratory of Optoelectronic Devices and Systems of Ministry of Education/Guangdong Province, College of Physics and Optoelectronic Engineering, Shenzhen University, Shenzhen 518060, China

³ International Collaborative Laboratory of 2D Materials for Optoelectronics Science and Technology of Ministry of Education, Institute of Microscale Optoelectronics, Shenzhen University, Shenzhen 518060, China

wjbao@szu.edu.cn

characteristics [3–6]. However, this method necessitates mandatory pre-fabrication hydrogen loading and post-fabrication annealing, thereby increasing both the time cost and potential risks associated with the process [7,8]. Additionally, the fiber coating has to be removed due to its opacity to UV laser, which compromises the fiber's mechanical strength and exacerbates heat accumulation during high-power laser operation, ultimately leading to degraded laser output performance. Recently, the femtosecond laser inscription technique utilizing a phase mask has emerged for CTFBG fabrication [9,10]. This method eliminates the requirement for hydrogen loading and thermal annealing [11–13], significantly reducing the fabrication cycle and gaining widespread application in the preparation of CTFBGs in double-clad fibers for SRS suppression. Nonetheless, the inherent reliance on phase masks imposes constraints on the grating parameters, such as wavelength, bandwidth, and length, while also limiting the inscription of gratings with large tilt angles [14].

In contrast, femtosecond laser direct writing technology provides a solution to the shortcomings of established phase mask-based techniques due to its high flexibility, which has been widely used in fields of sensing [15,16], communication [17,18], and lasers [19,20] over the past two decades. For fiber Bragg gratings (FBGs) inscription, this technology mainly includes three forms: point-by-point (P-b-P) [21], line-by-line (L-b-L) [22], and plane-by-plane (Pl-b-Pl) [23]. FBGs inscribed using Pl-b-Pl technology typically demonstrate superior performance, exhibiting the lowest insertion loss and highest spectral performance due to their uniform planar modulation characteristics. This renders Pl-b-Pl technology ideal for the fabrication of high-quality CTFBGs for fiber laser applications. However, the Pl-b-Pl technology is challenging to implement, particularly in fibers with large core diameters. Duan et al [24]. demonstrated the fabrication of Pl-b-Pl CTFBGs in single-mode fibers using a femtosecond laser combined with the slit shaping method. However, the incomplete core coverage leads to relatively high insertion loss and restricts this method's applicability to fibers with substantially larger core diameters. To date, no additional studies on planar CTFBGs have been reported. Besides, other existing spatial light shaping techniques [25–29] are typically capable of extending the focal region of femtosecond laser to cover a larger core area, thus also showing potential for fabricating Pl-b-Pl CTFBGs. However, these focal extensions reduce energy density, consequently diminishing the reflectivity per modulation plane, which pose challenges to the preparation of chirped gratings. Moreover, to compensate for the energy density reduction, the source power must be increased substantially, which introduces additional fabrication instabilities and risks.

Nonetheless, planar modulation implementation may draw inspiration from waveguide fabrication techniques. Based on the processing characteristics of femtosecond laser in silica-based materials, waveguides with various light-guiding properties have been fabricated by partially overlapping laser-induced refractive index modification (RIM) regions [30–32]. These studies indicate that the refractive index (RI) changes in these areas interact with each other through spatial overlapping of multiple femtosecond laser-induced RIM regions, thereby enabling the construction of highly customizable RIM profiles. Similarly, by designing specific RIM profiles, various planar modulations can be realized in optical fibers with different core diameters. In our previous work [33], we have demonstrated the fabrication of planar FBGs with high spectral performance in double-clad fibers with a core/cladding diameter of $14/250\,\mu m$ using a femtosecond laser overlap-controlled multilayer line-by-line (OCML-LBL) technique, and successfully applied them as cavity mirrors in fiber lasers. Owing to its high flexibility and excellent modulation uniformity, this technique also shows great potential for fabricating high-quality P1-b-P1 CTFBGs, and is therefore expected to provide a reliable approach for femtosecond laser direct writing of SRS suppressors.

In this work, we propose the fabrication of CTFBGs using the OCML-LBL technology. The planar modulation is achieved by precisely overlapping the multiple layers of Type II modulation induced by the femtosecond laser, which is effectively verified through RI measurements of the

grating cross section. The enhancement in the spectral performance of CTFBGs through this planar modulation is experimentally validated. The spectral characteristics of the CTFBGs are confirmed through both simulations and experiments, and the influence of various parameters on their spectral properties is investigated. Filtering applications with bandwidths ranging from 38 nm to 109 nm and filtering efficiency up to 99.96% are successfully demonstrated. The fabricated CTFBGs exhibit insensitivity to temperature, axial strain, and bending, confirming their excellent anti-interference capability and spectral stability. Furthermore, application tests within a laser system demonstrate the outstanding SRS suppression capability of the fabricated CTFBGs.

2. Fabrication setup and method

As shown in Fig. 1, the CTFBGs were experimentally fabricated by using a frequency-doubled femtosecond laser (KY-Vibre, Keyun) with a pulse duration of 200 fs, a central wavelength of 515 nm, and a repetition rate of 1 MHz in a single-mode fiber (SMF, G652D, YOFC) with a core/cladding diameter of $9/125 \mu m$ through a 100x oil-immersion objective (NA = 1.25). The SMF was fixed on an assembled 3D high-precision air-bearing translation stage (QFL100-100XY and RBN150V-5, AUS-PRECISION) which can move the fiber towards x, y and z-axis. Here, by precisely controlling the 3D translation stage and femtosecond laser through programming, the OCML-LBL technology was realized to fabricate planar grating area. The inset (a) and (b) exhibit the fabrication process. Here, at the starting position of CTFBG, we define the coordinates of the core's central point as (0,0,0). Firstly, the femtosecond laser was focused at $(0, -7 \,\mu\text{m})$, $-7 \,\mu m$) below the core, and then scanned the first tilted line along the x-y plane with a tilt angle θ to the y-axis and a component of 14 µm on the y-axis. Secondly, the laser point was back to the starting position and moved up along the z-axis by a distance of $d = 2 \mu m$. Then, the laser point was focused at $(0, -7 \,\mu\text{m}, -5 \,\mu\text{m})$ and scanned the second tilted line with the same parameters, and so on. Thus, the first scanning plane P_1 with seven lines and a modulation size of $L \times D$ could be obtained. Subsequently, the SMF was moved a distance of Λ_1 along the x-axis, and the laser point scanned the second plane from the position of $(\Lambda_1, -7 \,\mu\text{m}, -7 \,\mu\text{m})$. In this way, a CTFBG

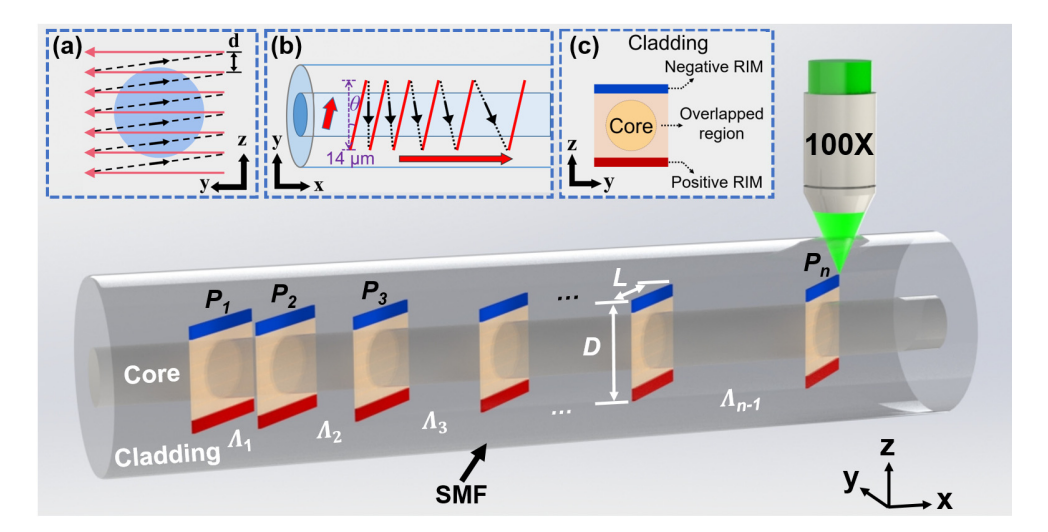


Fig. 1. Schematic diagram for fabricating a CTFBG in SMF using femtosecond laser OCML-LBL technology. Inset: (a) z-y plane and (b) x-y plane of the trajectory schematic of the laser spot; (c) schematic diagram of refractive index modulation (RIM) in the cross-section of the fiber.

composed of n modulation planes (P_1, P_2, \ldots, P_n) could be finally obtained, where the pitch between each plane $(\Lambda_1, \Lambda_2, \ldots, \Lambda_{n-1})$ was linearly increased. The CTFBG features a uniform planar modulation across the fiber core, with its cross-sectional RIM distribution shown in inset (c). The underlying mechanism and the rationale behind the parameter settings will be provided in the section 3.2(below). By precisely controlling the parameters of the grating, such as pitch of Λ , tilt angle of θ , chirp rate of δ , and total length, customized transmission and reflection spectra of CTFBG could be realized. Additionally, note that by varying the length (L) and the number of layers of the lines, planar CTFBGs could be inscribed in fibers with different core diameters.

3. Simulation, fabrication, and characterization of the CTFBGs

3.1. Numerical simulation and fabrication of the CTFBGs

The principles of CTFBGs have been analyzed in detail in previous works [3,6]. Based on these theoretical analyses, we conducted numerical simulations of the CTFBG. All simulations were performed based on the standard single-mode communication fiber, where the core and cladding refractive indices/diameters were set to 1.452/8 um and 1.446/125 um, respectively. Figure 2(a) shows the difference in the transmission and reflection spectra of a tilted fiber Bragg grating (TFBG) with a tilt angle of 4° under chirping (2.5 nm/cm) and no chirping conditions. In the case without chirping, the transmission spectrum of the TFBG exhibits a comb-like envelope formed by numerous narrowband loss peaks, with each loss peak corresponding to a coupled cladding mode. When chirping is introduced, these narrowband peaks broaden, resulting in significant overlap between them, and ultimately forming a smooth broadband transmission loss envelope. Since the cladding modes are dissipated during transmission in the single-mode fiber, only the Bragg reflection of the core mode is observed in the reflection spectrum, which also broadens due to the chirping effect. As shown in Fig. 2(b), as the tilt angle of the CTFBG increases, the transmission envelope undergoes a blue shift, and the bandwidth and depth of the envelope exhibit a certain degree of increase and decrease, respectively. Meanwhile, due to the decrease in the coupling coefficient of the core mode with increasing tilt angle, the intensity of the Bragg reflection also decreases. Here, the chirp rates are fixed at 2.5 nm/cm. Figure 2(c) presents the spectra of the CTFBGs with different chirp rates. Here, the tilt angles are fixed at 8°. When the chirp rate is small, the transmission spectrum shows a residual comb-like envelope. As the chirp rate gradually increases, the comb-like envelope transitions into a smooth broadband envelope, and the bandwidth and depth of the envelope increase and decrease accordingly. As the chirp rate increases, the bandwidth and intensity of the Bragg reflection also increase and decrease, respectively. As shown in Fig. 2(d), with an increase in the refractive index modulation amplitude, both the depth of the transmission envelope and the Bragg reflection intensity increase, while the bandwidth remains largely unchanged. Here, the tilt angles are fixed at 4°.

Simulation analysis reveals the hybrid nature of the CTFBG, incorporating spectral characteristics of chirped fiber Bragg grating (CFBG) and TFBG, which are verified by the following experiment. As shown in Fig. 3, CFBG, TFBG, and CTFBG were fabricated separately using OCML-LBL technology. The initial pitch, fabrication energy, scanning speed, and total length for all three FBGs were 1.07 μ m, 14 nJ, 0.15 mm/s, and 1 mm, respectively. Unless otherwise specified, all subsequent experiments used the same parameter settings as above. Figure 3(a)–3(c) illustrate the fabrication principles of each: CFBG consists of multiple planes parallel to the y-axis with linearly increased pitches, TFBG consists of multiple planes with a tilt angle θ to the y-axis and equal pitches, and CTFBG consists of multiple planes with a tilt angle θ to the y-axis and linearly increased pitches. As shown in the transmission spectra in Fig. 3(d), the CFBG (with a tilt angle of 0° and a chirp rate of 150 nm/cm) exhibits a filtering bandwidth of 15 nm within the Bragg waveband, with an average transmission depth of > -10 dB and negligible insertion loss. Here, the filtering bandwidth is defined as the wavelength difference between the turning points of the slopes at both ends of the transmission loss envelope, and the average transmission depth is

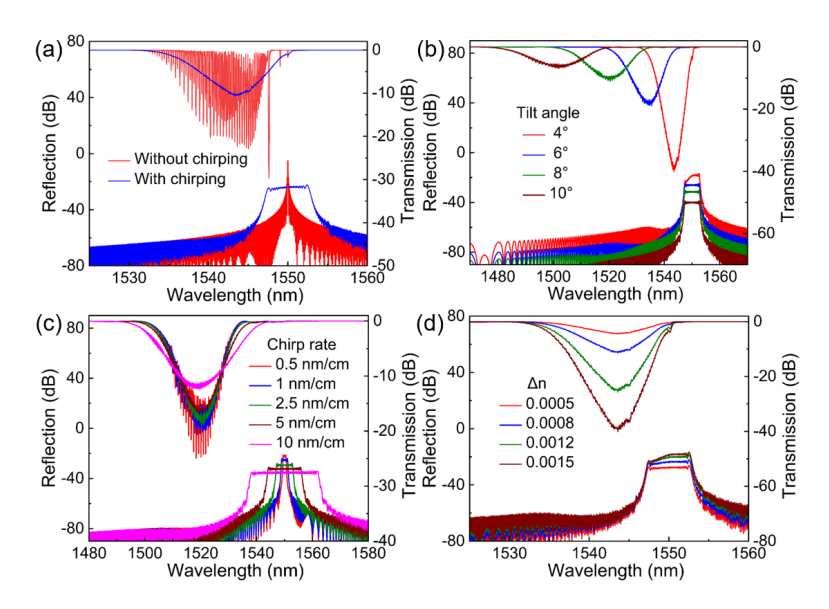


Fig. 2. Simulated transmission and reflection spectra of (a) TFBG and CTFBG with tilt angles of 4°, (b) CTFBGs with different tilt angles, (c) CTFBGs with different chirp rates, and (d) CTFBGs with different refractive index modulation amplitudes.

defined as the average transmission intensity within the filtering bandwidth. The TFBG (with a tilt angle of 15° and a chirp rate of 0) shows a broadband comb-like transmission spectrum with a filtering bandwidth of 80 nm and a dip of -6.5 dB. The CTFBG (with a tilt angle of 15° and a chirp rate of 150 nm/cm) broadens the numerous narrowband cladding modes present in the transmission spectrum of the TFBG, causing these modes to overlap and ultimately transforming the comb-like spectrum into a smooth and continuous one. The filtering bandwidth is widened to 95 nm, with the transmission dip decreasing to -3.0 dB. The reflection spectra in Fig. 3(d) reveal that the CFBG exhibits a significant (~-15 dB) broadband Bragg reflection centered at ~1550 nm, the TFBG shows a weaker (<-20 dB) narrowband Bragg reflection at ~1550 nm, whereas the CTFBG demonstrates the weakest (~-30 dB) broadband Bragg reflection at ~1550 nm, suggesting a negligible back-reflection for this device. Additionally, in the reflection spectrum of the CFBG, the two broadband reflection signals around 1400 nm and 1475 nm—similar to Bragg reflection—are potentially induced by femtosecond laser modulation, though the specific mechanism behind their formation has not yet been reported. However, with the introduction of chirp and tilt, the intensity of these undesired reflection signals is significantly suppressed, and thus they do not have a notable impact on the reflection characteristics of the CTFBG. Here, the insertion losses of CFBG, TFBG and CTFBG are all 0.3 dB.

3.2. Spectral performance optimized by OCML-LBL technology

Realized by the planar RIM, the proposed OCML-LBL technology can effectively reduce the insertion loss of fiber gratings. Using a digital holographic microscopy (SHR-1602, Shanghai University), we measured and investigated the changes in cross-sectional RI induced by different numbers of modulation layers, thereby verifying the planar modulation mechanism of the OCML-LBL technique. Due to equipment limitations, only the cross-sectional RI of uniform fiber Bragg gratings (UFBGs, with tilt angles of 0° and chirp rates of 0) were measured. As shown in the side-view microscopic images in Fig. 4(a₁)-4(a₄), under identical processing conditions of a pulse energy of 14 nJ and a scanning speed of 0.15 mm/s, UFBGs with 1, 2, 4, and 7 modulation layers

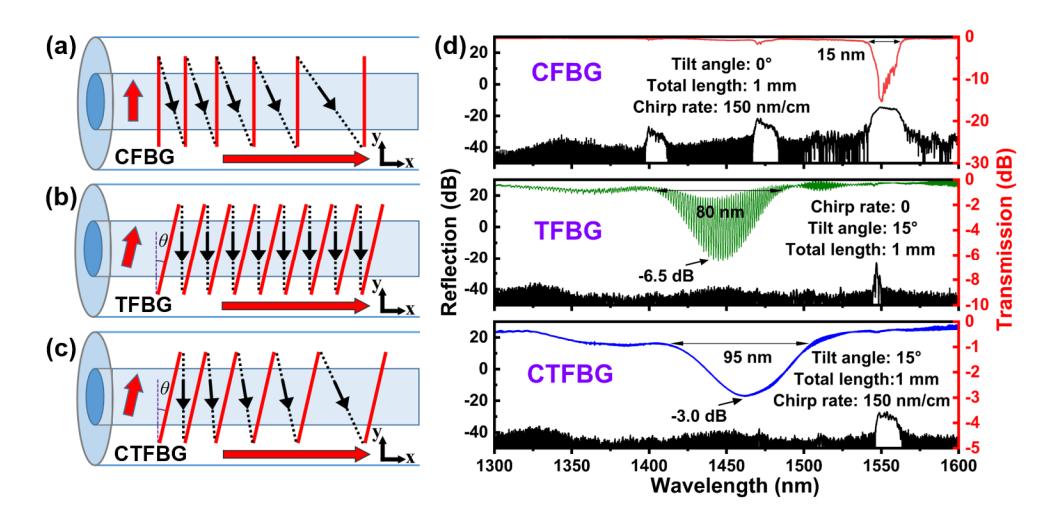


Fig. 3. Schematic diagrams of the fabrication principles of (a) CFBG, (b) TFBG, and (c) CTFBG. (d) transmission and reflection spectra of the obtained CFBG (θ = 0, δ = 150 nm/cm), TFBG (θ = 15°, δ = 0) and CTFBG (θ = 15°, δ = 150 nm/cm) fabricated by using femtosecond laser OCML-LBL technology.

were fabricated, exhibiting respective depths of 4 μm, 6 μm, 10 μm, and 16 μm. Figure 4(b₁)-4(b₄) exhibit the cross-sectional microscopic images of the SMF under different numbers of modulation layers. As shown in Fig. $4(b_1)$, when the number of modulation layers is one, a Type II modulation structure can be observed, consisting of a micro-trench and a material accumulation region beneath it. The micro-trench is formed at the focal region of the femtosecond laser, while the material accumulation region (as indicated by the glowing white horizontal bar in Fig. 4(b₁)) is generated beneath it as a result of the stress-induced effect [34], which compresses the material downward from the focal area. In contrast to typical waveguide fabrication in bulk materials [34], the in-fiber femtosecond laser inscription using a high numerical aperture objective results in the material accumulation region of Type II modulation predominantly forming beneath the laser focus region rather than on its lateral sides [25,35]. As shown in Fig. $4(b_2)-4(b_4)$, with the increase in the number of layers, the material compressed downward by each subsequent layer fills the micro-trench formed by the previous layer. Thus, only the micro-trench from the final layer and the material accumulation region from the first layer remain observable. Ultimately, these two structures are completely isolated in the cladding outside the core, while a relatively mild material modification region covering the core is formed in between (see Fig. $4(b_4)$). Figure $4(c_1)-4(c_4)$ demonstrate the accordingly changes in cross-sectional RI, validating the homogeneous planar RIM of the core based on the OCML-LBL technology. Under the given processing parameters, when the number of modulation layers was 1, the depths of the negative and positive RIMs were approximately identical (~2 µm). When an additional layer was added—i.e., the laser focus was raised by 2 µm—the positive RIM induced by the new layer overlapped with the negative RIM induced by the previous layer, resulting in a superposition in the middle region. As the number of layers increased to 7, a uniform overlapped RIM with a depth of ~12 μm formed in the center, while the positive RIM of the first layer and the negative RIM of the last layer (each $\sim 2 \,\mu m$) were isolated outside the fiber core, as shown in Fig. $4(c_4)$. Thus, by controlling the length $(14 \,\mu\text{m})$ and the number of layers (7) of the modulation lines, homogeneous planar modulation within the SMF core was achieved. Under different processing parameters, better overlapping effects can be realized by optimizing the interval d of the layers. Note that through adjusting the parameters of the modulation lines, the OCML-LBL technique can be adapted for grating fabrication in optical

fibers with various core diameters [33]. Compared to the core of SMF without FBG, the average RIM of the core region in Fig. $4(c_4)$ is about 1.0×10^{-3} .

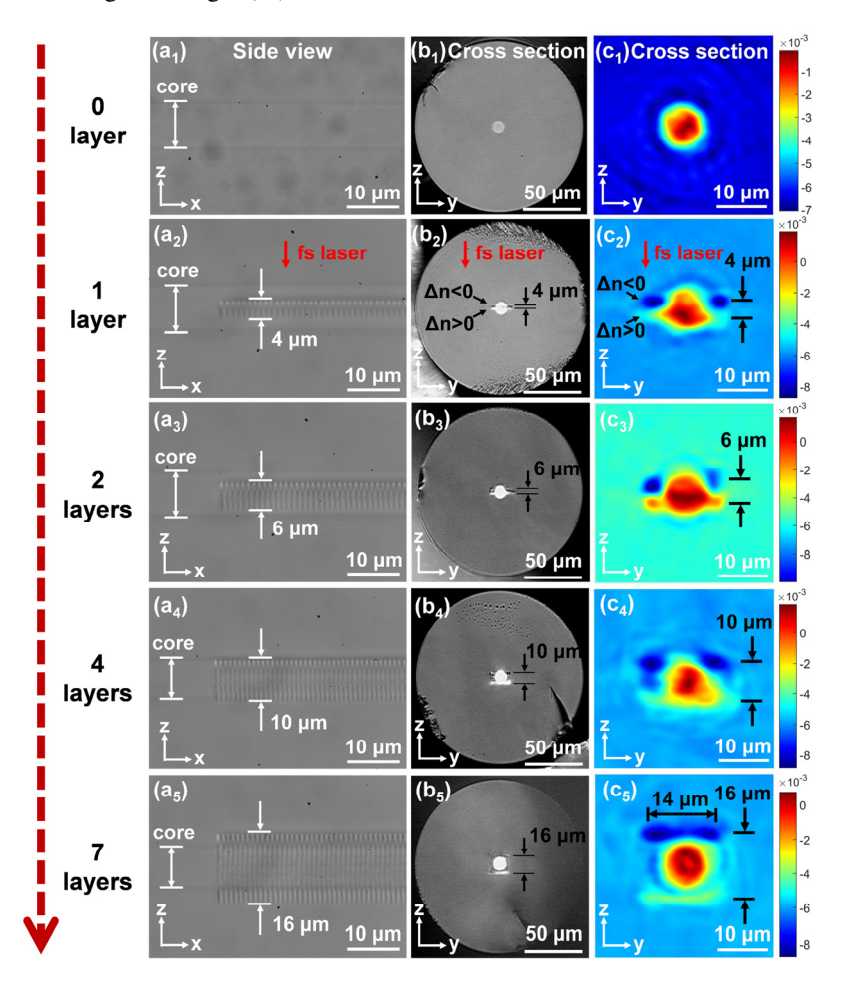


Fig. 4. (a) Side-view microscopic images, (b) cross-sectional microscopic images, and (c) cross-sectional refractive index distribution of the UFBGs with different modulation layers of 0, 1, 2, 4, and 7.

The reduction of type-II-modulation-induced scattering and the optimization of CTFBG spectral performance realized by the planar modulation based on the OCML-LBL technology have been verified. As shown in Fig. 5(a), CTFBGs with the same length of 1 mm and different modulation layers of 1, 2, 4, 7, 8, and 9 were fabricated using a chirp rate of 10 nm/cm and a tilt angle of 8°. Compared with the single-layer CTFBG, the multi-layer CTFBGs exhibited a significantly enhanced spectral contrast (coupling depth/insertion loss). The differences in central wavelength and bandwidth between the single- and multi-layer CTFBGs in the transmission spectra mainly arise from different cladding mode excitations induced by structural differences in the grating modulation plane. As shown in Fig. 5(b), with the increase of layer number, the spectral losses (including both long- and short-wavelength losses) first increase and then decrease. This is because, for the 2- and 4-layer CTFBGs compared with the 1-layer CTFBG, the pronounced negative modulation (the primary source of insertion loss) located above their modulation plane still remained in the core, while additional modulation regions were introduced, leading to extra losses. When the number of layers increases to 7 or more, the negative modulation

structure was completely isolated into the cladding, resulting in a uniform positive modulation in the core and thereby significantly reducing the scattering loss of the CTFBG. In addition, the uniform planar modulation covering the entire fiber core can suppress high-order cladding mode coupling, thereby reducing short-wavelength loss in the grating [36,37] and significantly improving the spectral contrast. To further verify this, we investigated the spectral performance of CTFBGs with different number of layers at the same coupling depth. As shown in Fig. 5(c), when the coupling depth reached the same level (-8 dB), the short- and long-wavelength losses in the transmission spectra were significantly reduced as the number of layers increased from 1 to 2, 4, and 7. When the number of layers reached 7, the planar modulation had already covered the fiber core, thus further increases to 8 and 9 layers provided no additional improvement. Here, the CTFBGs had grating lengths of 5.0 mm, 2.5 mm, 1.7 mm, 1.6 mm, 1.6 mm, and 1.6 mm, respectively. Figure 5(d) shows the trend in spectral losses with increasing layer number. From 1 to 7 layers, the short-wavelength loss decreased from 2.50 dB to 0.64 dB, and the long-wavelength loss decreased from 1.16 dB to 0.39 dB, resulting in a minimal difference of only 0.25 dB. When the number of layers increased to 8 and 9, the short-wavelength losses were 0.67 dB and 0.66 dB, respectively, while the long-wavelength losses were 0.36 dB and 0.43 dB—values that show negligible change compared to the 7-layer case. Considering fabrication efficiency, 7 modulation layers were selected for CTFBG fabrication in all subsequent experiments. Here, the long-wavelength losses were defined as the average transmission loss over the 1560-1600 nm range, and the short-wavelength losses were averaged over the 1300-1400 nm range.

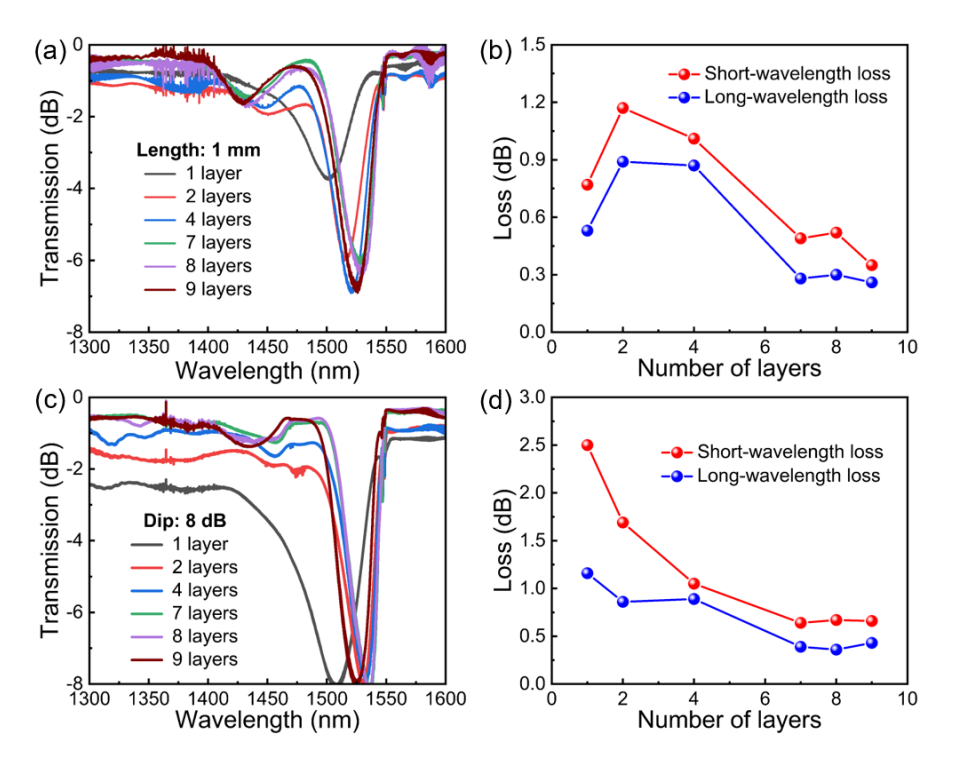


Fig. 5. Transmission spectra and spectral losses of the CTFBGs with different modulation layers of 1, 2, 4, 7, 8 and 9, respectively, when (a)-(b) the grating lengths are 1 mm and (c)-(d) the dips are 8 dB.

3.3. Spectral properties of the CTFBGs

The influence of different tilt angles θ on the spectra of the proposed CTFBGs was investigated. As shown in Fig. 6(a)-6(d), CTFBGs with tilt angles of 4°, 8°, 12°, and 16° were fabricated, using the same fabrication energy of 14 nJ, chirp rate of 20 nm/cm, and total length of 5 mm. As shown in Fig. 6(e), when the tilt angle was 4°, the CTFBG had a transmission dip of -34.3 dB, corresponding to a filtering efficiency of 99.96%, a 3dB-bandwidth of 38 nm and a central wavelength of 1549.4 nm. Here, the 3 dB-bandwidth is defined as the wavelength difference between the two points where the filtering envelope intersects a line positioned 3 dB below the insertion loss (long-wavelength loss) level. As the tilt angle increased to 8°, 12°, and 16°, the transmission dip decreased to -21.0 dB, -16.5 dB, and -14.0 dB, respectively, with corresponding filtering efficiency of 99.2%, 97.8%, and 96.0%, the 3dB-bandwidth broadened to 47 nm, 78 nm, and 109 nm, respectively, and the central wavelength shifted to 1533.8 nm, 1498.5 nm and 1439.5 nm. These trends are in good agreement with the simulation results. The presence of residual comb-like spectra in large-tilt-angle CTFBGs is attributed to the larger spacing between cladding mode coupling peaks in the short-wavelength region, resulting in insufficient spectral broadening under the same chirp amount. Therefore, by controlling the tilt angle θ , broadband-adjustable filtering applications with bandwidths ranging from 38 nm to over 100 nm and filtering efficiencies consistently above 95% could be achieved. Note that each CTFBG exhibited an insertion loss of only -0.8 dB. From the reflection spectra in Fig. 6(e), it could be observed that as the tilt angle increased, the intensity of the Bragg reflection gradually weakened from \sim -20 dB to \sim -40 dB, which was beneficial for reducing the back-reflection.

Subsequently, the influence of different chirp rates on the spectra of CTFBGs was investigated. As shown in Fig. 7, CTFBGs with chirp rates of 10 nm/cm, 20 nm/cm, and 30 nm/cm were fabricated using the same pulse energy of 14 nJ, tilt angle of 12°, and total length of 5 mm. When the chirp rate was 10 nm/cm, the transmission dip of the CTFBG was -14.3 dB (corresponding to a filtering efficiency of 96.3%), with a 3dB-bandwidth of 59 nm. As the chirp rate increased to 20 nm/cm and 30 nm/cm, the transmission dip of the CTFBG decreased to -11.9 dB and -9.2 dB (corresponding to filtering efficiencies of 93.5% and 88.0%), respectively, and the 3dB-bandwidth increased to 65 nm and 72 nm, respectively. Because of the relatively short grating length, increasing the chirp rate caused only a minor change in the central wavelength of the CTFBG. Therefore, by adjusting the chirp rate of the CTFBG, the filtering applications with different bandwidths at specific central wavelengths could be achieved. Additionally, as observed from the reflection spectrum, with the linear increase of the chirp rate, the Bragg reflection bandwidth of the CTFBG also increased linearly, while the reflection intensity gradually weakened from about -20 dB to less than -30 dB.

In many practical filtering applications, back-reflection signal will adversely affect the system. For example, in high-power fiber laser systems, sufficiently strong back-reflected light may damage upstream components. Moreover, in the field of communications, echo signals can induce inter-channel crosstalk, thereby increasing the bit error rate. In our research, by adjusting the initial pitch Λ_1 of the CTFBG, the Bragg back-reflection could be flexibly controlled. As shown in Fig. 8, when the initial pitch Λ_1 increased linearly from 1.000 µm to 1.035 µm, 1.070 µm, and 1.105 µm, the Bragg reflection wavelength of the CTFBG increased linearly from 1448 nm to 1498 nm, 1548 nm, and 1598 nm, and the filtering wavelength of the CTFBG also exhibited a nearly linear increase from 1431 nm to 1479 nm, 1529 nm, and 1578 nm. Therefore, based on Fig. 6 and Fig. 8, it could be concluded that by simultaneously controlling the initial pitch Λ_1 and tilt angle θ of the CTFBG, the positions of the filtering wavelength and Bragg back-reflection wavelength, as well as the interval between them, can be flexibly customized. This will be beneficial to control the back-reflection signal outside the operating band of the system to alleviate its influence. The difference between the filtering wavelength and the Bragg reflection wavelength increases with the initial pitch, as it is proportional to the grating period according to

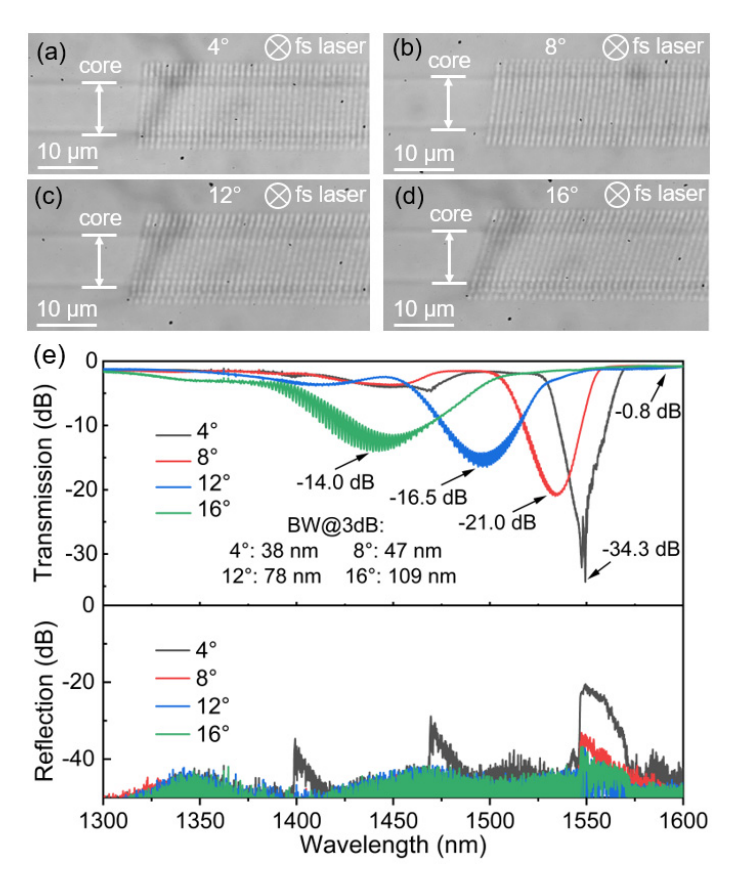


Fig. 6. Top-view microscopic images of the CTFBGs with different tilt angles of (a) 4° , (b) 8° , (c) 12° , and (d) 16° , respectively; (e) transmission and reflection spectra of the CTFBGs with different tilt angles of 4° , 8° , 12° , and 16° , respectively. BW@3dB: 3dB-bandwidth.

the phase-matching condition [38]. Furthermore, with the increase of the Bragg wavelength, the coupling depth of the CTFBG decreases due to the reduction in the coupling coefficient, while the bandwidth increases [39]. And as a result, it becomes more challenging to fabricate CTFBGs with broader bandwidths at shorter wavelengths.

3.4. Spectral stability tests of the CTFBGs

Additionally, we have tested the spectral stability of the prepared CTFBG under various conditions of temperature, axial strain, and bending. Here, the tested CTFBG had a tilt angle of 8° , a chirp rate of 20 nm/cm, and a total length of 5 mm. For each kind of experiment, three independent measurements were conducted. The spectral response from one representative measurement is presented, along with the averaged spectral parameter variations from all three repetitions. As shown in Fig. 9(a₁), the temperature response of the CTFBG was measured using a high-precision column oven (LCO 102), with the temperature varied from 30°C to 90°C and maintained for 5 minutes at each set point. Figure 9(a₂) indicates that the average central wavelength shift of the CTFBG was merely 0.59 nm over the entire temperature range, which is negligible compared to its 3 dB bandwidth of 47 nm. For axial strain testing, one end of the CTFBG was fixed, while the other was mounted on a one-dimensional manual translation stage, enabling controlled axial strain from 0 to 2000 μ E, as shown in Fig. 9(b₁). The results in Fig. 9(b₂) show an average wavelength shift of only 1.14 nm over this strain range, which remains relatively small. Bending

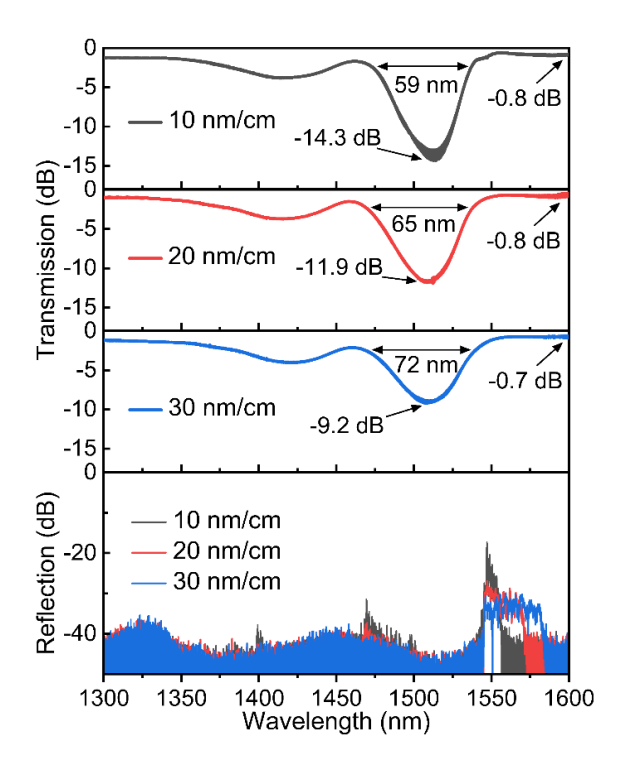


Fig. 7. Transmission and reflection spectra of the CTFBGs with different chirp rates of 10 nm/cm, 20 nm/cm, and 30 nm/cm, respectively.

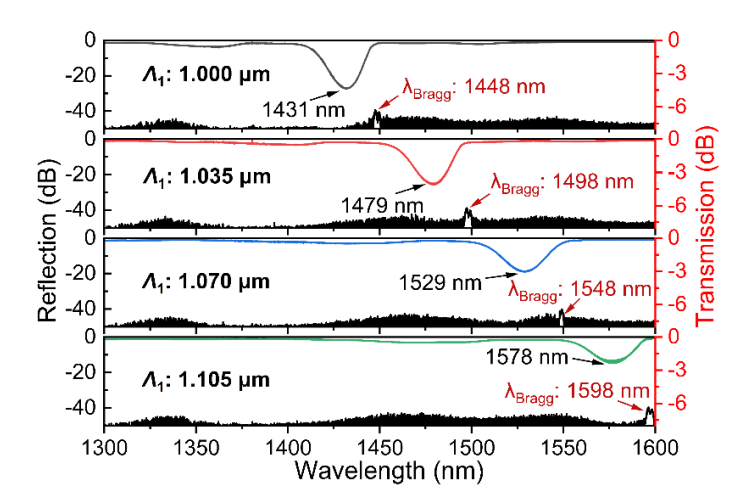


Fig. 8. Transmission and reflection spectra of the CTFBGs with different initial pitches of $1.000 \, \mu m$, $1.035 \, \mu m$, $1.070 \, \mu m$, and $1.105 \, \mu m$, respectively.

response was characterized using a custom-designed curvature plate, with curvature values ranging from 0 to $1/2.5 \, \mathrm{cm}^{-1}$, corresponding to bending radii from infinity to $2.5 \, \mathrm{cm}$, as shown in Fig. 9(c₁). Figure 9(c₂) shows the variation of the transmission dip of the CTFBG under different bending conditions, indicating an overall change within 0.42 dB, which had a minimal influence compared to the transmission depth of -22 dB. The overall results in Fig. 9 demonstrate that the

prepared CTFBG exhibits excellent spectral stability under significant variations in temperature, axial strain, and bending, revealing a good interference resistance of this device.

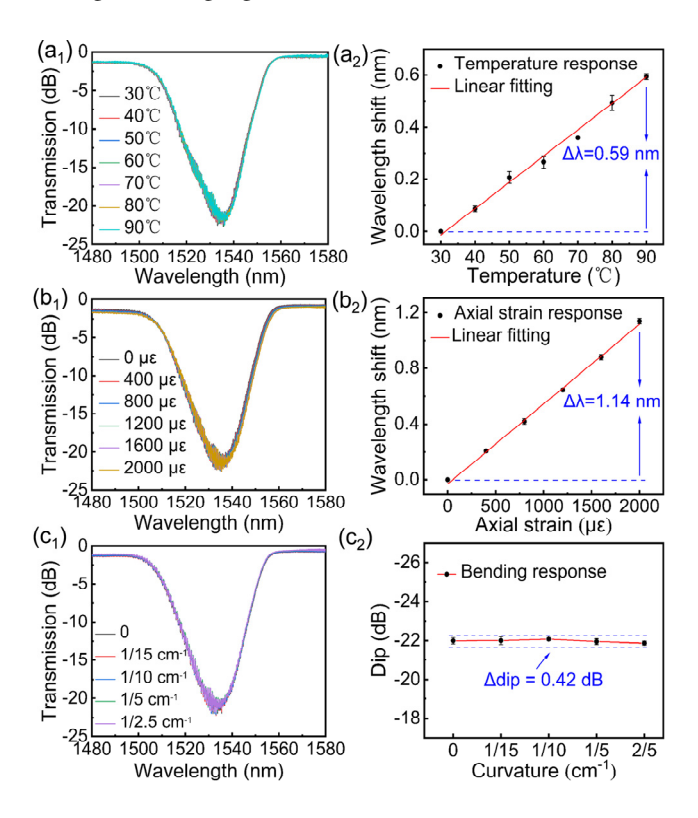


Fig. 9. Spectral stability tests of the obtained CTFBG. (a) Temperature response from 30° C to 90° C. (b) Axial strain response from 0 to $2000 \,\mu\text{E}$. (c) Bending response: bending radius from infinity (no bending) to $2.5 \,\text{cm}$, corresponding to the curvature from 0 to $2/5 \,\text{cm}^{-1}$.

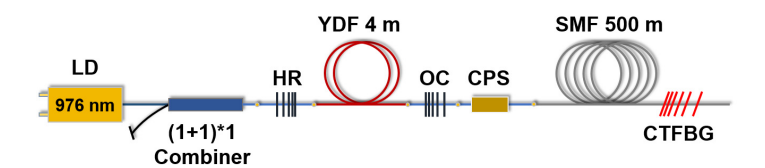


Fig. 10. A laser system for evaluating the SRS suppression effect of CTFBG.

4. SRS suppression in a laser system

Furthermore, we have evaluated the effectiveness of the CTFBG in SRS suppression within a fiber laser system. As shown in Fig. 10, the laser system comprises a pump laser diode (LD, 976 nm, 60 W output power), a $(1+1)\times 1$ combiner (input: $105/125\,\mu m$ multi-mode fiber, output: 10/130 passive double-clad fiber), a high-reflectivity FBG (HR, central wavelength: $1063.7\,nm$, reflectivity: 99.9%, bandwidth: $2\,nm$), a 4-meter-long ytterbium-doped gain fiber (LMA-YDF-10/130-M), and an output-coupling FBG (OC, central wavelength: $1064.0\,nm$, reflectivity: 10%, bandwidth: $1\,nm$). The fiber type for both the HR and OC is LMA-GDF-10/130-M. A cladding power stripper (CPS) was used to remove residual pump light, and a 500-meter-long

SMF (SMF-28e, Corning) was added after the CPS to reduce the SRS threshold. The output characteristics of the laser were then measured without and with the inclusion of the CTFBG. As shown in Fig. 11(a), the fabricated CTFBG features a 3 dB-bandwidth of 27 nm, a filtering depth of 15.5 dB, and a central wavelength of 1117.3 nm, which aligns closely with the Stokes light wavelength generated by the 1064 nm Yb-doped laser. The initial pitch of this CTFBG was 0.783 µm and its total length was only 0.9 mm. As stated in Section 3.3, it is more challenging to obtain a larger bandwidth when fabricating CTFBGs at shorter wavelengths. To achieve an appropriate bandwidth, the CTFBG fabricated here was given a tilt angle of 10°. Due to the use of a supercontinuum source (SC-5, YSL Photonics) with notable power fluctuations during fabrication, the original transmission spectrum exhibited significant jitter. A smoothed fitting was therefore applied to enhance clarity. As shown in Fig. 11(b), in the absence of the CTFBG, SRS began to appear in the output spectrum once the pump power exceeded 20.7 W. As the pump power increased from 20.7 W to 26.3 W, the Stokes component grew steadily to approximately -35 dBm, only ~15 dB below the signal light peak (around −20 dBm), which had a noticeable impact on the laser's performance. After integrating the fabricated CTFBG at the system, the SRS signal was effectively suppressed, as shown in Fig. 11(c). Even as the pump power increased from 20.7 W to 26.3 W, the Stokes signal remained below -70 dBm, yielding a suppression ratio exceeding 50 dB relative to the signal light peak. The slight increasing of the signal light peak's side lobes is attributed to $\sim 4\%$ Fresnel reflection at the fiber end of the CTFBG, which modified the cavity length and increased the number of longitudinal modes. Figure 11(d) shows the thermal profile of the CTFBG captured using an infrared thermometer. The CTFBG was mounted on the optical platform without any additional thermal management. At the maximum pump power of 26.3 W, the temperature of the CTFBG was measured to be 33.1°C, indicating its good power-handling capability.

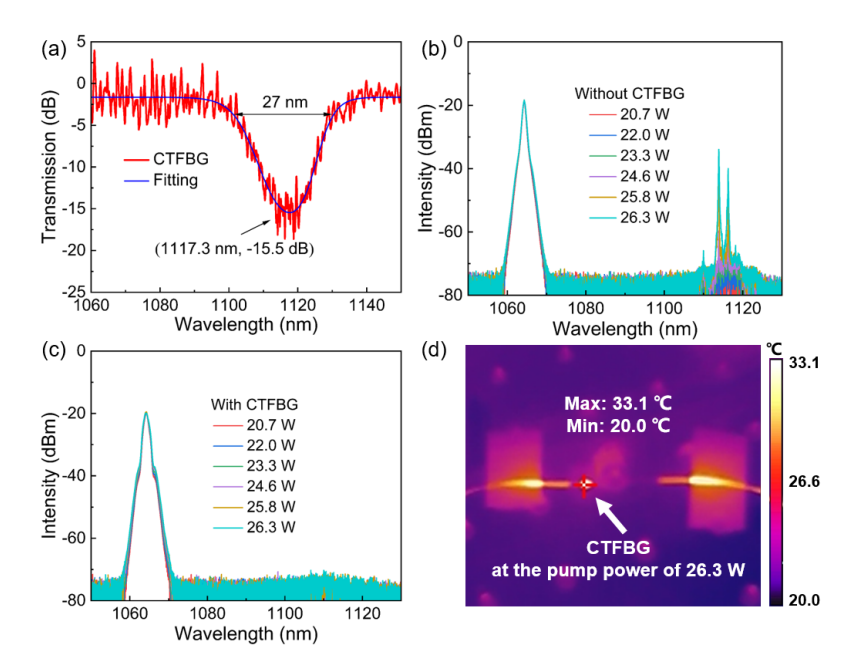


Fig. 11. (a) Transmission spectrum of the CTFBG used in the SRS suppression; (b) laser output spectra without the CTFBG; (c) laser output spectra with the CTFBG; (d) thermal image of the CTFBG at a pump power of 26.3 W.

5. Conclusion

In conclusion, we have proposed and demonstrated a flexible and adjustable technology, i.e., femtosecond laser overlap-controlled multilayer line-by-line (OCML-LBL) technology, for fabricating stimulated Raman scattering (SRS) suppressors based on chirped and tilted fiber Bragg gratings (CTFBGs). The cross-sectional refractive index changes induced by the gratings were measured, which verified a homogeneous planar modulation with a magnitude of 1.0×10^{-3} in the core region. The influence of varying modulation layers on the transmission spectrum of CTFBG was investigated, confirming the optimization of insertion loss achieved through the OCML-LBL technology. By adjusting the tilt angle, CTFBGs with 3dB-bandwidths ranging from 38 nm to 109 nm and efficiencies from >90% to >99.9% could be realized. The filtering bandwidth at a specific wavelength could be flexibly controlled by adjusting the chirp rate. Additionally, through adjusting the initial pitch, the wavelength of the Bragg back-reflection could be flexibly customized to reduce its adverse effects on the practical applications. The temperature, axial strain, and bending tests demonstrated the fabricated CTFBG's good anti-interference capability and spectral stability. Moreover, experimental tests within a laser system confirm that the fabricated CTFBG possesses excellent SRS suppression performance and power-handling capability. In the future, by flexibly changing the modulation structure, the OCML-LBL technology is promising to fabricate high-quality CTFBGs in fibers with larger core diameters for high-power SRS suppression.

Funding. National Key Research and Development Program of China (2023YFB3209500); National Natural Science Foundation of China (U22A2088); Shenzhen Science and Technology Program (JCYJ20241202124226032, JCYJ20220818095800001); Shenzhen Key Laboratory of Ultrafast Laser Micro/Nano Manufacturing (ZDSYS2022060610 0405013); Scientific Foundation for Youth Scholars of Shenzhen University (806-0000340610).

Disclosures. The authors declare no conflicts of interest.

Data availability. Data underlying the results presented in this paper are not publicly available at this time but may be obtained from the authors upon reasonable request.

References

- D. Nodop, C. Jauregui, F. Jansen, et al., "Suppression of stimulated Raman scattering employing long period gratings in double-clad fiber amplifiers," Opt. Lett. 35(17), 2982–2984 (2010).
- Q. Hu, X. Zhao, X. Tian, et al., "Raman suppression in 5 kW fiber amplifier using long period fiber grating fabricated by CO2 laser," Opt. Laser Technol. 145, 107484 (2022).
- 3. M. Wang, Y. J. Zhang, Z. F. Wang, *et al.*, "Fabrication of chirped and tilted fiber Bragg gratings and suppression of stimulated Raman scattering in fiber amplifiers," Opt. Express **25**(2), 1529–1534 (2017).
- 4. K. Jiao, J. Shu, H. Shen, *et al.*, "Fabrication of kW-level chirped and tilted fiber Bragg gratings and filtering of stimulated Raman scattering in high-power CW oscillators," High Power Laser Sci. Eng. 7, e31 (2019).
- H. Song, D. Yan, W. Wu, et al., "SRS suppression in multi-kW fiber lasers with a multiplexed CTFBG," Opt. Express 29(13), 20535 (2021).
- F. Liu, T. Guo, C. Wu, et al., "Wideband-adjustable reflection-suppressed rejection filters using chirped and tilted fiber gratings," Opt. Express 22(20), 24430–24438 (2014).
- S. J. Mihailov, C. Hnatovsky, N. Abdukerim, et al., "Ultrafast laser processing of optical fibers for sensing applications," Sensors 21(4), 1447 (2021).
- A. V. Tokarev, G. G. Anchutkin, S. V. Varzhel, et al., "UV-transparent fluoropolymer fiber coating for the inscription of chirped Bragg gratings arrays," Opt. Laser Technol. 89, 173–178 (2017).
- 9. H. Li, X. Y. Ye, M. Wang, et al., "Robust femtosecond-written chirped and tilted fiber Bragg gratings for Raman filtering in multi-kW fiber lasers," Opt. Lett. 48(14), 3697–3700 (2023).
- 10. H. Li, J. B. Chen, X. Y. Ye, *et al.*, "Raman suppression in high-power fiber oscillators by femtosecond-written chirped and tilted fiber Bragg gratings," Opt. Express **31**(25), 41875–41886 (2023).
- D. Grobnic, C. W. Smelser, S. J. Mihailov, et al., "Fiber Bragg gratings with suppressed cladding modes made in SMF-28 with a femtosecond IR laser and a phase mask," IEEE Photonics Technol. Lett. 16(8), 1864–1866 (2004).
- K. M. Yang, J. He, C. R. Liao, et al., "Femtosecond laser inscription of fiber bragg grating in twin-core few-mode fiber for directional bend sensing," J. Lightwave Technol. 35(21), 4670–4676 (2017).
- 13. J. He, B. J. Xu, X. Z. Xu, *et al.*, "Review of femtosecond-laser-inscribed fiber bragg gratings: fabrication technologies and sensing applications," Photonics Sens. 11(2), 203–226 (2021).
- 14. H. Li, M. Wang, B. Y. Wu, et al., "Femtosecond laser fabrication of chirped and tilted fiber Bragg gratings for stimulated Raman scattering suppression in kilowatt-level fiber lasers," Opt. Express 31(8), 13393–13401 (2023).

- A. Lacraz, A. Theodosiou, and K. Kalli, "Femtosecond laser inscribed Bragg grating arrays in long lengths of polymer optical fibres; a route to practical sensing with POF," Electron. Lett. 52(19), 1626–1627 (2016).
- M. H. Wang, P. S. Salter, F. P. Payne, et al., "Single-mode sapphire fiber Bragg grating," Opt. Express 30(9), 15482–15494 (2022).
- 17. D. Z. Tan, Z. Wang, B. B. Xu, *et al.*, "Photonic circuits written by femtosecond laser in glass: improved fabrication and recent progress in photonic devices," Adv. Photonics 3(02), 024002 (2021).
- 18. S. Kroesen, W. Horn, J. Imbrock, *et al.*, "Electro-optical tunable waveguide embedded multiscan Bragg gratings in lithium niobate by direct femtosecond laser writing," Opt. Express **22**(19), 23339–23348 (2014).
- G. Della Valle, S. Taccheo, R. Osellame, et al., "1.5 μm single longitudinal mode waveguide laser fabricated by femtosecond laser writing," Opt. Express 15(6), 3190–3194 (2007).
- Y. W. Duan, P. Dekker, E. Jaatinen, et al., "Narrow linewidth DFB waveguide laser fabricated via ultrafast laser inscription," IEEE Photonics Technol. Lett. 26(24), 2499–2502 (2014).
- L. Chen, C. L. Fu, Z. H. Cai, et al., "High-quality fiber Bragg grating inscribed in ZBLAN fiber using femtosecond laser point-by-point technology," Opt. Lett. 47(14), 3435–3438 (2022).
- K. M. Zhou, M. Dubov, C. B. Mou, et al., "Line-by-line fiber Bragg grating made by femtosecond laser," IEEE Photonics Technol. Lett. 22(16), 1190–1192 (2010).
- A. Theodosiou, J. Aubrecht, P. Peterka, et al., "Er/Yb double-clad fiber laser with fs-laser inscribed plane-by-plane chirped FBG laser mirrors," IEEE Photonics Technol. Lett. 31(5), 409

 –412 (2019).
- 24. T. X. Duan, X. Y. Li, R. H. Wang, et al., "Femtosecond laser plane-by-plane inscription of chirped and tilted fiber Bragg gratings," J. Lightwave Technol. 42(17), 6083–6089 (2024).
- J. F. Wu, X. Z. Xu, C. R. Liao, et al., "Optimized femtosecond laser direct-written fiber Bragg gratings with high reflectivity and low loss," Opt. Express 31(3), 3831–3838 (2023).
- P. Lu, S. J. Mihailov, H. M. Ding, et al., "Plane-by-plane inscription of grating structures in optical fibers," J. Lightwave Technol. 36(4), 926–931 (2018).
- X. Y. Li, F. Y. Chen, W. J. Bao, et al., "Beam-shaping device-free femtosecond laser plane-by-plane inscription of high-quality FBGs," Opt. Laser Technol. 161, 109226 (2023).
- C. H. Gao, R. Zhao, X. D. Lu, et al., "Femtosecond laser parallel plane-by-plane inscribed fiber Bragg grating based on superimposed blazed grating phase masks," Opt. Express 33(12), 25959–25969 (2025).
- 29. C. H. Gao, R. Zhao, B. Y. Wu, *et al.*, "Femtosecond laser direct writing large-area fiber Bragg grating based on diaphragm shaping," Opt. Express **32**(11), 18582–18593 (2024).
- 30. Y. Y. Wang, L. J. Zhong, K. Y. Lau, *et al.*, "Precise mode control of laser-written waveguides for broadband, low-dispersion 3D integrated optics," Light: Sci. Appl. **13**(1), 130 (2024).
- A. G. Okhrimchuk, A. V. Shestakov, I. Khrushchev, et al., "Depressed cladding, buried waveguide laser formed in a YAG: Nd3 + crystal by femtosecond laser writing," Opt. Lett. 30(17), 2248–2250 (2005).
- A. Okhrimchuk, V. Mezentsev, A. Shestakov, et al., "Low loss depressed cladding waveguide inscribed in YAG:Nd single crystal by femtosecond laser pulses," Opt. Express 20(4), 3832–3843 (2012).
- 33. Y. Fan, W. J. Bao, Q. Li, et al., "Fiber Bragg grating inscribed in large mode area double-clad fiber using femtosecond laser multi-layer line-by-line technology," J. Lightwave Technol. 43(3), 1400–1405 (2025).
- 34. F. Chen and J. R. V. de Aldana, "Optical waveguides in crystalline dielectric materials produced by femtosecond-laser micromachining," Laser Photonics Rev. 8(2), 251–275 (2014).
- 35. B. J. Xu, J. He, X. Z. Xu, *et al.*, "Simultaneous measurement of torsion and strain at high temperature by using a highly birefringent cladding fiber Bragg grating," Opt. Express **30**(16), 28710–28719 (2022).
- 36. T. Erdogan, "Cladding-mode resonances in short- and long-period fiber grating filters," J. Opt. Soc. Am. A **14**(8), 1760–1773 (1997).
- 37. J. Thomas, N. Jovanovic, R. G. Becker, *et al.*, "Cladding mode coupling in highly localized fiber Bragg gratings: modal properties and transmission spectra," Opt. Express **19**(1), 325–341 (2011).
- 38. J. Albert, L. Y. Shao, and C. Caucheteur, "Tilted fiber Bragg grating sensors," Laser Photonics Rev. 7(1), 83–108 (2013).
- 39. T. Erdogan, "Fiber grating spectra," J. Lightwave Technol. 15(8), 1277-1294 (1997).